ADVANCED MATERIALS

www.advmat.de

3D Nanofabrication via Chemo-Mechanical Transformation of Nanocrystal/Bulk Heterostructures

Mingliang Zhang, Jiacen Guo, Yao Yu, Yaoting Wu, Hongseok Yun, Davit Jishkariani, Wenxiang Chen, Nicholas J. Greybush, Christian Kübel, Aaron Stein, Christopher B. Murray, and Cherie R. Kagan**

Planar nanocrystal/bulk heterostructures are transformed into 3D architectures by taking advantage of the different chemical and mechanical properties of nanocrystal and bulk thin films. Nanocrystal/bulk heterostructures are fabricated via bottom-up assembly and top-down fabrication. The nanocrystals are capped by long ligands introduced in their synthesis, and therefore their surfaces are chemically addressable, and their assemblies are mechanically "soft," in contrast to the bulk films. Chemical modification of the nanocrystal surface, exchanging the long ligands for more compact chemistries, triggers large volume shrinkage of the nanocrystal layer and drives bending of the nanocrystal/bulk heterostructures. Exploiting the differential chemo-mechanical properties of nanocrystal and bulk materials, the scalable fabrication of designed 3D, cell-sized nanocrystal/bulk superstructures is demonstrated, which possess unique functions derived from nanocrystal building blocks.

3D patterning on the micro- or nanoscale can realize unique device functionalities not achievable by conventional 2D lithographic methods, such as creating nanorobots that capture and deliver cargo for therapeutics and impurity scavenging and chiral metasurfaces for enantiomer-selective catalysis and sensing.[1–4] An important strategy is to realize shape transformations by folding 2D lithographically defined structures into 3D configurations.[5] Most reports use mechanically "soft" organic materials.[6–9] Although structurally successful, they generally lack electronic, optical, and magnetic functionalities, and are typically larger than 100 µm in size. In contrast, inorganic materials have desired functionalities,[10–12] yet they are mechanically "hard" and their deformations require either processing at an elevated temperature[13] or via high-energy ion-beam bombardment.[14,15]

Solution-processable colloidal nanocrystals (NCs) are hybrid systems composed of inorganic cores and organic/inorganic ligand shells.[16] The combination of their size-dependent physical properties and low-cost processability is driving exploration of NC-based electronic, optical, and magnetic devices.[17–21] To achieve targeted device performances, NC films are often assembled "bottom-up," to define their nano- to mesoscale structure, and patterned "top-down," to control their micro- to macroscale structure.[22–24] Here, we exploit the chemical addressability of the NC ligand shell, "soft" mechanical properties of NC assemblies, and unique physical properties of the NC cores to create large-scale, 3D, functional NC/bulk bilayer heterostructures suitable for cell-sized machines/devices. Chemical modification of the NC surface, exchanging long ligands for more compact chemistries, decreases the interparticle distance, triggers a large volume shrinkage of the NC layer, and drives bending of the heterostructures. We construct design rules to demonstrate the versatility of this fabrication approach and to create multiple 3D superstructures. By selecting superparamagnetic NC building blocks, we realize 3D "claws" that are actuated by an external magnetic field.

As a basic element, NC/bulk bilayer nanowires are fabricated (**Figure 1**a), by sequentially evaporating Ti and spin-coating Au NCs in a tri-layer resist template patterned via scalable nanoimprint lithography (NIL) with 3 µm long nanowire trenches.[25] Each nanowire trench is 60 nm wide in the top thermal resist layer (unless otherwise specified, noted as *w*), and has an undercut structure in the middle poly(methyl glutarimide) (PMGI) layer. Due to the different deposition characteristics, the evaporated Ti has a width defined by *w*, while the spin-coated Au NCs occupy the entire PMGI undercut area,

Dr. M. Zhang, Dr. W. Chen, Prof. C. R. Kagan
Department of Electrical and Systems Engineering
University of Pennsylvania
Philadelphia, PA 19104, USA
E-mail: kagan@seas.upenn.edu

Dr. M. Zhang, Dr. Y. Wu, Dr. H. Yun, Dr. D. Jishkariani, Prof. C. B. Murray, Prof. C. R. Kagan
Department of Chemistry
University of Pennsylvania
Philadelphia, PA 19104, USA
E-mail: cbmurray@sas.upenn.edu

Dr. M. Zhang, J. Guo, Y. Yu, Dr. N. J. Greybush, Prof. C. B. Murray, Prof. C. R. Kagan
Department of Materials Science and Engineering
University of Pennsylvania
Philadelphia, PA 19104, USA

Dr. C. Kübel
Karlsruhe Nano Micro Facility and Institute of Nanotechnology
Karlsruhe Institute of Technology
76344 Eggenstein-Leopoldshafen, Germany

Dr. A. Stein
Center for Functional Nanomaterials
Brookhaven National Laboratory
Upton, NY 11973, USA

The ORCID identification number(s) for the author(s) of this article can be found under https://doi.org/10.1002/adma.201800233.

DOI: 10.1002/adma.201800233

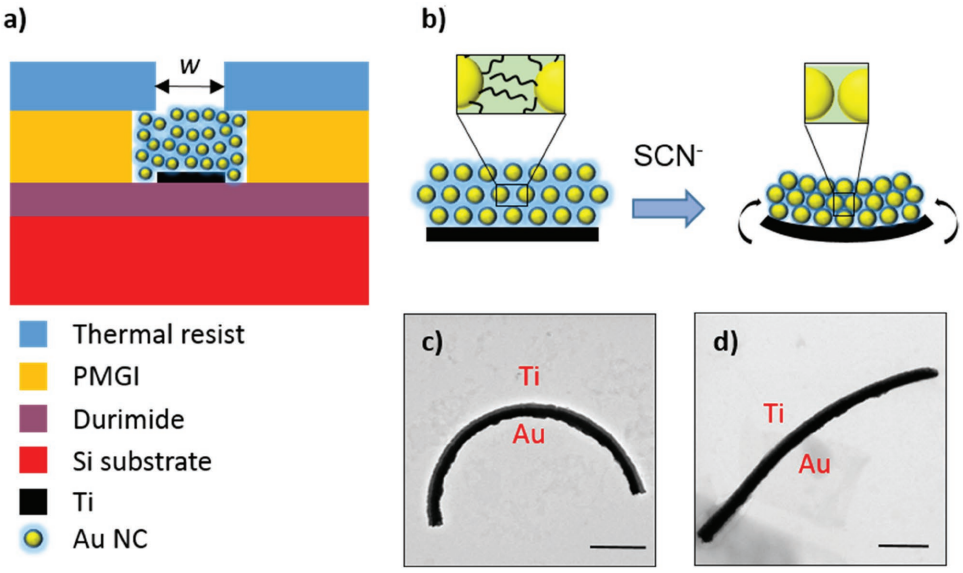

Figure 1. Fabrication of Au NC/Ti heterostructure nanowires and their bending. a) Schematic of the bilayer nanowire fabrication through sequential Ti evaporation and Au NC spin-coating onto a tri-layer resist film patterned by NIL. b) Schematic of an initially OLA-capped Au NC/Ti bilayer nanowire bending upon LE with NH_4SCN. The LE process replaces the long organic chains separating neighboring NCs, causing neighboring NCs to touch, and the bilayer nanowire to bend. c,d) TEM images of the bilayer nanowire with (c) LE and without (d) LE (scale bar: 500 nm). In both images, the nanowires lie on substrates on their sides.

typically with a width 50 nm larger than w. A bottom resist layer of Durimide allows us to ultimately harvest the nanowires from the substrate surface by dissolving the resist layer.

The Au NCs have an average core diameter of 4.9 ± 0.3 nm and an oleylamine (OLA) shell thickness of 0.8 ± 0.2 nm, leading to an OLA ligand/Au volume ratio of 1.3. After lift-off of the thermal resist, the long OLA ligands are replaced with compact SCN^- ligands via a ligand exchange (LE) process in which the samples are immersed in a solution of the new ligand. Previous work has shown that LE of similar-size, OLA-capped Au NCs with SCN^- ligands creates a 56% volume reduction in Au NC films[26] and nanowires.[17] This volume change is significantly larger than the 10% volume change of an NC assembly using LE with DNA chemistry[27] and thus drives a large bending effect in the NC/bulk bilayer nanowires (Figure 1b), as seen in transmission electron microscopy (TEM) images (Figure 1c). While LE of NC/bulk nanowires shows a large bending effect, without LE nanowires only have a slight curvature (Figure 1d), possibly due to the residual stress introduced by the deposition processes. Cross-sectional images and 3D renderings constructed by electron tomography confirm the NC/bulk morphology and bending and the large volume reduction in the NC layer upon LE (Figure S1, Supporting Information).

The bending of the nanowires can be described using a well-established bilayer model.[28] Here, we assume that LE has introduced an initial compressive strain of ε_0 in the length direction of the Au NC layer, also known as the misfit strain between the Au NC/Ti layers, causing the nanowire to bend with a curvature $1/\rho$ (**Figure 2**a). The ratio between the nanowire thickness h and ρ can be expressed as

$$\frac{h}{\rho} = \frac{\varepsilon_0}{f(k,t)} \tag{1}$$

where

$$f(k,t) = \frac{1}{2} + \frac{1}{6}\left[k(1-t)^3 + t^3\right]\left[\frac{1}{k(1-t)} + \frac{1}{t}\right] \tag{2}$$

Here k is the Young's modulus ratio between the Au NC and the Ti bulk layers, and t is the ratio of the Ti layer thickness a_{Ti} to the total bilayer thickness h. While it is difficult to control the thickness of the Au NC layer deposited in the templates (Figure S2, Supporting Information), a_{Ti} can be tuned to modulate t and study the thickness dependence of the bending effect (Figure S3, Supporting Information). At least five nanowires are measured for each t point, and their h/ρ values are plotted in Figure 2b. We fit the average h/ρ values at different t points found experimentally to the classic bilayer model. More careful treatment can be conducted by taking into account the variation of measured h/ρ (Figure S4, Supporting Information), revealing a distribution of ε_0 and k values as shown in Figure 2c. Consequently, ε_0 takes the value of 0.064 ± 0.018, consistent with the earlier reported length reduction of 0.09 upon LE for single Au NC nanowires.[17] For comparison, bending created by the differential thermal expansion of an inorganic copper/steel bi-metallic strip only has a misfit strain of 0.005 with a 1000 K temperature change.[29] The large misfit strain is consistent with the large Au NC volume reduction, providing a large driving force to bend the bilayer nanowire.

The fitting process further yields k between 0.0019 and 0.0079 with 1σ significance, corresponding to a Au NC layer elastic modulus between 210 and 870 MPa (the elastic modulus of bulk crystalline Ti is 110.3 GPa),[29] orders of magnitude lower than the bulk Au modulus (79 GPa).[29] The decrease in modulus for NC layers is consistent with nanoporous Au systems formed by selective etching of Ag in a Au–Ag alloy.[30] However,

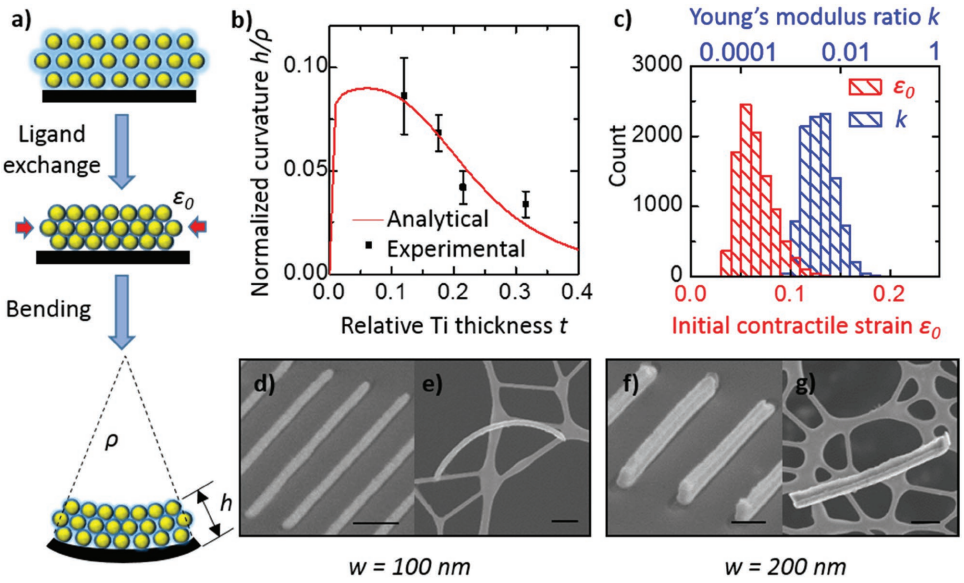

Figure 2. Dependence of the bending effect on the nanowire's geometrical parameters. a) Illustration of misfit strain ε_0 and of nanowires with thickness h bending upon LE, creating curvature $1/\rho$. b) Experimental (black dots) dependence of the bending effect, characterized by the normalized curvature h/ρ, on the relative Ti layer thickness normalized by the overall nanowire thickness h. Fitting (red curve) of the average experimental value of h/ρ to a stressed bilayer model. c) Distribution of the fitted misfit strain ε_0 (red) and the Young's modulus ratio between the Au NC layer and Ti layer (blue) by assigning a normal distribution to the measured h/ρ data in (b). SEM images of bilayer nanowires fabricated from d,e) $w = 100$ nm and f,g) $w = 200$ nm templates. d–g) Nanowires as fabricated on a Durimide layer (d,f) and upon release and deposition on a lacey carbon grid (e,g) (scale bar: 500 nm).

in those systems, a larger modulus of 2.7–3.2 GPa is reported. The discrepancy cannot be explained by the different relative Au density, as our Au NC layers have an even higher Au density.[17] However, unlike systems built from tens-of-micrometer-sized grains, our Au NC layer has a coherence length of only 15.8 nm (Figure S5, Supporting Information), suggesting limited grain growth during LE from the original 4.9 nm NCs. Due to atomic disorder, grain boundaries typically have a reduced elastic modulus, and this is especially the case for the current Au NC system considering that it is constructed initially from randomly oriented NCs. Therefore, it suggests that the grain boundaries in our nanometer grain size Au NC systems play an essential role in determining the ensemble elastic modulus, and therefore contribute to its smaller value. Importantly, the orders-of-magnitude smaller Young's modulus in the "soft" Au NC layer facilitates the shape deformation of the bilayer.

In the following discussion, the Ti layer thicknesses are maintained at 20 nm, and unless otherwise noted, the same fabrication procedure is used. The nanowire trench width w is modulated to also control the bending effect. For example, scanning electron microscopy (SEM) images show that the 100 nm template yields nanowires with a similar bending curvature as does the 60 nm template (Figure 2d,e). However, as w increases to 200 nm, the nanowires appear almost straight (Figure 2f,g). Careful inspection reveals different cross-sectional profiles for these two samples that arise from interfacial, energetic differences in lift-off (Figure S6, Supporting Information). The large-w nanowires are found to have an NC layer 2.5 times as thick as the small-w counterparts (100 nm thick), leading to their smaller curvature.

Taking advantage of the "rules" to create bending upon LE of NC/bulk bilayer heterostructures, 3D cell-sized structures are designed with different curvatures at different locations by changing the NC layer thickness through the modulation of w. As an example, we fabricated curled-L structures with two orthogonally patterned nanowire segments L_w (w = 150 nm, 4 µm long) and L_t (w = 60 nm, 19 µm long) over large areas (**Figure 3**a; Figures S7 and S8, Supporting Information). There is a 500 nm wide, smoothly curved transition region at the junction point to prevent stress at the corner. Consistently, the wider segment L_w appears to have a larger thickness than L_t (Figure S8c, Supporting Information), in turn leading to different bending behavior once released. We suspend the curled-L structures upon release in N-methyl pyrrolidone and study their 3D structures by bright-field optical microscopy. At an elevated temperature (90 °C), Brownian motion exceeds gravitational forces, and the structures tumble frequently, revealing an unambiguous 3D morphology (Figure 3b–d and Movie S1, Supporting Information). As expected the smaller-w L_t region curves and forms a loop whereas the larger-w L_w region remains a straight short tip. The loop has a radius of 2.6 µm, slightly larger than the average radius of curvature for nanowires with a 20 nm Ti layer (ρ = 2.2 µm; Figure 2b, and Figure S3c, Supporting Information), due to the flat transition region on the junction side of L_t (Figure S8d, Supporting Information).

Increasing in design complexity, Figure 3e shows an example of a claw structure. Macrosized claws/grippers have already been reported to capture large objects,[31] while cell-sized claws could be useful in trapping microorganisms. A "+" sign-shaped 2D pattern with four 5 µm long arms is designed and fabricated over large area, with a similar smoothly curved transition region in the center (Figures S7 and S9a, Supporting Information). Once released, the four arms curl up toward the NC side, forming a claw structure (Figure 3f–h;Figure S9b and Movie S2,

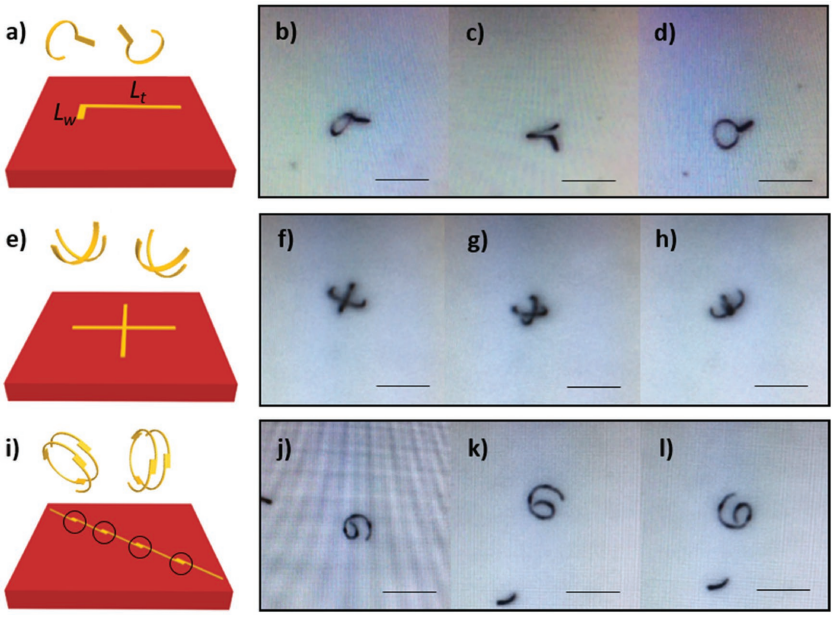

Figure 3. Various 3D NC/bulk bilayer structures created by bending. a,e,i) Schematics of transformations from planar to 3D structures with the yellow color representing the Au NC/bulk heterostructure and b–d,f–h,j–l) optical microscopy images of 3D structures suspended in solution captured at different times for curled-L structures (a–d), claw structures (e–h), and helical structures (i–l). Scale bar: 10 µm.

Supporting Information). Owing to the large bending curvature, these claws are less than 10 µm in size, making them suitable to interact with similarly sized tumor cells and bacteria. As a demonstration, these claws can wrap around 2.5 µm silica beads, with their arms following the curved bead surface (Figure S9c,d, Supporting Information). In the future, the surface chemistry of these claws could be modified to allow their transfer to physiologically benign media, to increase their binding affinity with cells, and to create a triggering process to realize a capturing motion. Another example is a helical structure, which is actively explored in realizing artificial motors[2] and chiral optical metamaterials.[1,3] Here, five 60 nm wide 4 µm long nanowires are aligned in the same direction, connected head-to-tail sequentially through junction rectangles (300 nm wide, 1 µm long) and each shifted by 240 nm from its predecessor in the transverse direction (Figure 3i; Figure S7, Supporting Information). Consequently, all five nanowires bend and form arcs, which are arranged helically (Figure 3j–l and Movie S3, Supporting Information). Among different 3D structure designs, more than 90% yields are achieved for both the curled-L and claw structures, and 40% yield for the more complicated helical structure. Each of the curled-L, claw, and helical patterns are fabricated using 2×2 cm^2 NIL stamps to yield approximately 10^7 3D structures (Figures S8 and S9, Supporting Information). Further scaling-up can be achieved using even larger stamps.[17,32] The 3D structures are stable and no structural degradation is observed during a 5 month storage period.

The versatility of this technique also lies in the choice of different functional NC building blocks to create 3D structures with unique physical properties. For example, superparamagnetic NCs are widely used in biomedical research, and their zero-remanence properties are crucial to prevent spontaneous magnetic-dipole-induced aggregation in solution.[10] Here, a superparamagnetic claw is fabricated from 12.6 ± 0.5 nm diameter $Zn_{0.2}Fe_{2.8}O_4$ NCs (**Figure 4**a), whose rotation can be magnetically actuated. The radius of curvature of the claw arms is 4.2 µm, larger than the Au-NC case, as the larger size of the $Zn_{0.2}Fe_{2.8}O_4$ NCs leads to a smaller ligand/NC core volume ratio and therefore a reduced initial compressive strain ε_0 upon LE. To demonstrate magnetic actuation, a permanent magnet is used to approach the claw suspension (starting at 0 s), generating a magnetic field of 150 Oe. In response, the magnetic claw stabilizes with their arms facing down on the substrate, and one of the angular bisectors aligned with the external field. From 10 to 30 s, the magnetic field is rotated clockwise and counterclockwise alternately, and the claw motion follows synchronously. The experiment indicates the dominant role of the magnetic interaction in the process. Further evidence lies in magnetic simulations, where the total magnetic energy is calculated for different external field orientations (Figure 4b,c) with respect to the claw structure. The highest energy occurs when the field is along two of the arms horizontally (Config. III), as here the field is transverse to the other two arms, forcing their magnetizations to align unfavorably (Figure S10, Supporting Information). Local energy minima occur at Config. I (field along the central axis) and Config. II (field aligned horizontally and at 45° to all the arms). Config. I has an energy 58.4 eV higher than Config. II, which can again be understood by the energy penalty of the transverse magnetization at the junction point (Figure S10, Supporting Information). The transformation between these two configurations requires overcoming an energy barrier of 103 eV at the midpoint ($\theta = 45°$, $\varphi = 45°$). Consistent with the experimental results, the simulation predicts that the claw will take Config. II to minimize the system energy, and that the energy barrier, which is much higher than the thermal fluctuation energy at room temperature, locks the claw in the stable state and forces it to move synchronously with the rotating magnetic field. The successful magnetic manipulation of the magnetic claw provides a route for cell manipulation/sorting, once these claws are attached to the cell surface.

In summary, we report a room-temperature, solution-based LE process that can chemo-mechanically transform planar NC/bulk heterostructures into 3D configurations. This 3D nanofabrication method features large structural transformation, mechanically soft structures, and flexibility in both structural design and NC selection, providing access to the unique physical properties of inorganic NCs and expanding the functionalities of existing organic natural/artificial 3D counterparts. Combined with NIL, the process is cost-effective and readily scalable.

Looking forward, due to the "hybrid" nature of the colloidal NCs, this technique creates cell-sized 3D structures, that can be designed to also possess optical, magnetic, chemical, and mechanical functionalities, not readily accessible in existing

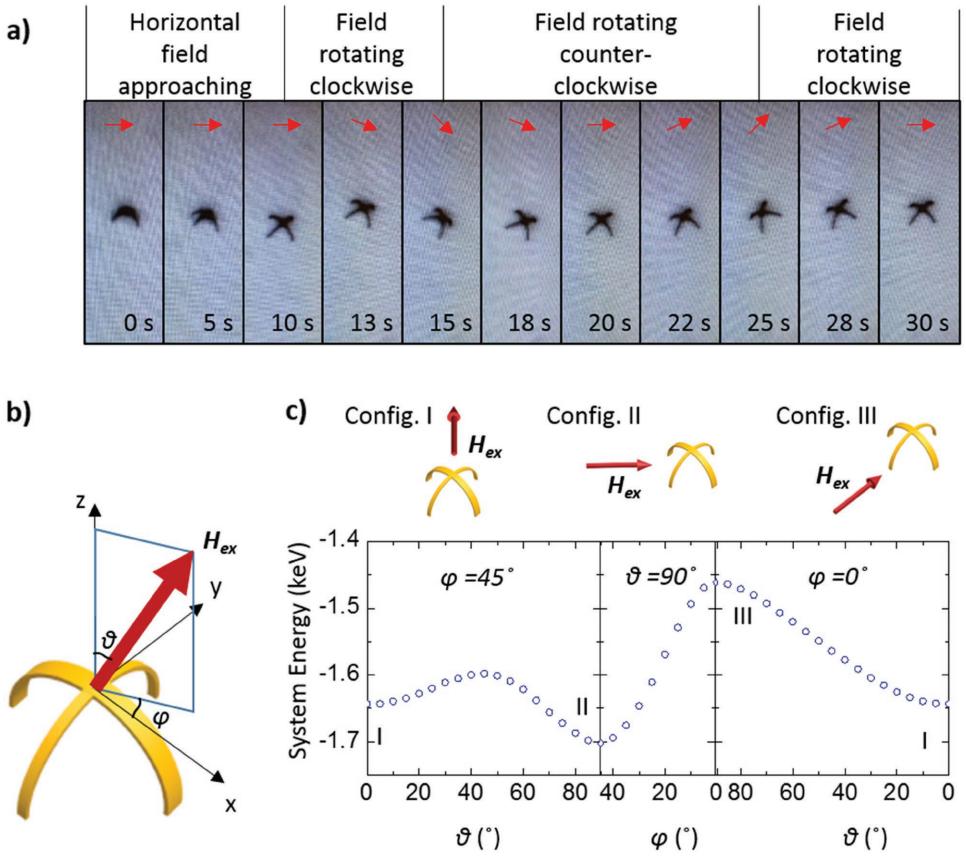

Figure 4. Magnetic claw in response to an external magnetic field. a) Optical microscopy images capturing the evolution of a magnetic claw with a permanent magnet approaching and aligned in the horizontal direction (0–10 s), rotating clockwise (10–15 s), counter-clockwise (15–25 s), and clockwise again (25–30 s). The red arrows represent the magnetic field orientations. b) Schematic of a magnetic claw with central axis oriented in the *z*-direction, and the *xy*-projection of the arms in *x*- and *y*-directions. The direction of the external field H_{ex} is defined by the angle θ with respect to the *z*-axis and the azimuthal angle φ. Here, the yellow color represents the magnetic NC/bulk heterostructure. c) The total magnetic system energy of the claw with different H_{ex} orientations. From left to right, the plots show the energy in situations of different θ at $\varphi = 45°$; different φ at $\theta = 90°$; and different θ at $\varphi = 0°$. The numbers in the plots label Config. I (field aligned with the central axis), Config. II (horizontal field aligned 45° with respect to the arms), and Config. III (horizontal field aligned with one pair of the arms), respectively.

folded structures of similar dimension.[13,33] The NC cores can be made of quantum dots,[16] superparamagnetic,[17] or catalytic[34] NCs, facilitating optical tracking, magnetic manipulation, or propulsion of the 3D structures, respectively. Their ligand chemistry can also be tailored, to exchange the OLA with bulkier groups[35] causing the NC layer to expand for reverse bending, or with photo-[36] or thermally[37] switchable compounds for reconfigurable, in-situ modulation of the 3D structures. The bulk metal layer can also be replaced with other inorganic or organic materials, allowing further tuning of the mechanical properties of the heterostructures. This technique promises to enable the design of functional, 3D structures, which have already shown their leading roles in a variety of fields including artificial motors, nanorobots, and chiral optical metasurfaces.

Supporting Information

Supporting Information is available from the Wiley Online Library or from the author.

Acknowledgements

M.Z. and J.G. contributed equally to this work. The authors thank Dr. J. Kikkawa for his help with magnetic field characterization. The authors are grateful for primary support of this work from the National Science Foundation (NSF) under Award No. CMMI-1562884 for heterostructure fabrication and characterization. Synthesis of Au nanocrystals was supported by National Science Foundation Grant No. NSF-561658, and synthesis of magnetic nanocrystals was supported by the Catalysis Center for Energy Innovation, an Energy Frontier Research Center funded by the U.S. Department of Energy, Office of Basic Energy Sciences, under Award No. DE-SC0001004. E-beam lithography to pattern the nanoimprint lithography master stamp was carried out at the Center for Functional Nanomaterials, Brookhaven National Laboratory, which is supported by the U.S. Department of Energy, Office of Basic Energy Sciences, under Contract No. DE-AC02-98CH10886. Electron tomography was performed at Karlsruhe Nano Micro Facility (KNMF), Karlsruhe Institute of Technology (KIT). M.Z. is grateful for support from the NatureNet Science Fellowship offered by the Nature Conservancy. J.G. was supported by Chinese Scholarship Counsel (CSC). Y.Y. was supported by Penn's Department of Materials Science and Engineering Masters Scholars Award. Scanning electron microscopy/FIB was performed in facilities supported by the NSF MRSEC Program under Award No. DMR-1720530.

Conflict of Interest

The authors declare no conflict of interest.

Keywords

3D patterning, folding, ligand chemistry, nanocrystal, nanoimprint lithography

Received: January 12, 2018
Revised: February 8, 2018
Published online: April 15, 2018

[1] H. H. Jeong, A. G. Mark, T. C. Lee, M. Alarcón-Correa, S. Eslami, T. Qiu, J. G. Gibbs, P. Fisher, *Nano Lett.* **2016**, *16*, 4887.
[2] S. Tottori, L. Zhang, F. Qiu, K. K. Krawczyk, A. Franco-Obregón, B. J. Nelson, *Adv. Mater.* **2012**, *24*, 811.
[3] J. K. Gansel, M. Thiel, M. S. Rill, M. Decker, K. Bade, V. Saile, G. von Freymann, S. Linden, M. Wegener, *Science* **2009**, *325*, 1513.
[4] Y. Kim, B. Yeom, O. Arteaga, S. J. Yoo, S. G. Lee, J. G. Kim, N. A. Kotov, *Nat. Mater.* **2016**, *15*, 461.
[5] Y. Zhang, F. Zhang, Z. Yan, Q. Ma, X. Li, Y. Huang, J. A. Rogers, *Nat. Rev. Mater.* **2017**, *2*, 17019.
[6] J. Kim, J. A. Hanna, M. Byun, C. D. Santangelo, R. C. Hayward, *Science* **2012**, *335*, 1201.
[7] S. J. Jeon, R. C. Hayward, *Adv. Mater.* **2017**, *29*, 1606111.
[8] A. S. Gladman, E. A. Matsumoto, R. G. Nuzzo, L. Mahadevan, J. A. Lewis, *Nat. Mater.* **2016**, *15*, 413.
[9] A. Cangialosi, C. Yoon, J. Liu, Q. Huang, J. Guo, T. D. Nguyen, D. H. Gracias, R. Schulman, *Science* **2017**, *357*, 1126.
[10] M. Zhang, C. M. Earhart, C. Ooi, R. J. Wilson, M. Tang, S. X. Wang, *Nano Res.* **2013**, *6*, 745.
[11] M. Zhang, X. Xie, M. Tang, C. S. Criddle, Y. Cui, S. X. Wang, *Nat. Commun.* **2013**, *4*, 1866.
[12] M. Zhang, N. Large, A. L. Koh, Y. Cao, A. Manjavacas, R. Sinclair, P. Nordlander, S. X. Wang, *ACS Nano* **2015**, *9*, 9331.
[13] T. G. Leong, P. A. Lester, T. L. Koh, E. K. Call, D. H. Gracias, *Langmuir* **2007**, *23*, 8747.
[14] Y. Mao, Y. Zheng, C. Li, L. Guo, Y. Pan, R. Zhu, J. Xu, W. Zhang, W. Wu, *Adv. Mater.* **2017**, *29*, 1606482.
[15] K. Chalapat, N. Chekurov, H. Jiang, J. Li, B. Parviz, G. S. Paraoanu, *Adv. Mater.* **2013**, *25*, 91.
[16] C. B. Murray, C. R. Kagan, M. G. Bawendi, *Annu. Rev. Mater. Sci.* **2000**, *30*, 545.
[17] M. Zhang, D. J. Magagnosc, I. Liberal, Y. Yu, H. Yun, H. Yang, Y. Wu, J. Guo, W. Chen, Y. J. Shin, A. Stein, J. M. Kikkawa, N. Engheta, D. S. Gianola, C. B. Murray, C. R. Kagan, *Nat. Nanotechnol.* **2017**, *12*, 228.
[18] F. Prins, D. K. Kim, J. Cui, E. D. Leo, L. L. Spiegel, K. M. McPeak, D. J. Norris, *Nano Lett.* **2017**, *17*, 1319.
[19] W. Chen, M. Tymchenko, P. Gopalan, X. Ye, Y. Wu, M. Zhang, C. B. Murray, A. Alu, C. R. Kagan, *Nano Lett.* **2015**, *15*, 5254.
[20] J. H. Choi, H. Wang, S. J. Oh, T. Paik, P. S. Jo, J. Sung, X. Ye, T. Zhao, B. T. Diroll, C. B. Murray, C. R. Kagan, *Science* **2016**, *352*, 205.
[21] C. R. Kagan, E. Lifshitz, E. H. Sargent, D. V. Talapin, *Science* **2016**, *353*, 885.
[22] Y. Wang, I. Fedin, H. Zhang, D. V. Talapin, *Science* **2017**, *357*, 385.
[23] T. Paik, H. Yun, B. Fleury, S. H. Hong, P. S. Jo, Y. Wu, S. J. Oh, M. Cargnello, H. Yang, C. B. Murray, C. R. Kagan, *Nano Lett.* **2017**, *17*, 1387.
[24] J. Yang, M. K. Choi, D. H. Kim, T. Hyeon, *Adv. Mater.* **2016**, *28*, 1176.
[25] W. Hu, M. Zhang, R. J. Wilson, A. L. Koh, J. S. Wi, M. Tang, R. Sinclair, S. X. Wang, *Nanotechnology* **2011**, *22*, 185302.
[26] A. T. Fafarman, S. H. Hong, H. Caglayan, X. Ye, B. T. Diroll, T. Paik, N. Engheta, C. B. Murray, C. R. Kagan, *Nano Lett.* **2013**, *13*, 350.
[27] T. S. Shim, Z. G. Estephan, Z. Qian, J. H. Prosser, S. Y. Lee, D. M. Chenoweth, D. Lee, S. J. Park, J. C. Crocker, *Nat. Nanotechnol.* **2017**, *12*, 41.
[28] S. Timoshenko, *J. Opt. Soc. Am.* **1925**, *11*, 233.
[29] R. E. Bolz, G. L. Tuve, *CRC Handbook of Tables for Applied Engineering Science*, 2nd ed., CRC Press, Boca Raton **1973**.
[30] T. J. Balk, C. Eberl, Y. Sun, K. J. Hemker, D. S. Gianola, *J. Microsc.* **2009**, *61*, 26.
[31] F. Ilievski, A. D. Mazzeo, R. F. Shepherd, X. Chen, G. M. Whitesides, *Angew. Chem., Int. Ed.* **2011**, *50*, 1890.
[32] M. Zhang, D. J. B. Bechstein, R. J. Wilson, S. X. Wang, *Nano Lett.* **2014**, *14*, 333.
[33] M. Z. Miskin, K. J. Dorsey, B. Bircan, Y. Han, D. A. Muller, P. L. McEuen, I. Cohen, *Proc. Natl. Acad. Sci. USA* **2018**, *115*, 466.
[34] S. Sundararajan, P. E. Lammert, A. W. Zudans, V. H. Crespi, A. Sen, *Nano Lett.* **2008**, *8*, 1271.
[35] D. Jishkariani, B. T. Diroll, M. Cargnello, D. R. Klein, L. A. Hough, C. B. Murray, B. Donnio, *J. Am. Chem. Soc.* **2015**, *137*, 10728.
[36] L. D. Zarzar, V. Sresht, E. M. Sletten, J. A. Kalow, D. Blankschtein, T. M. Swager, *Nature* **2015**, *518*, 520.
[37] X. He, M. Aizenberg, O. Kuksenok, L. D. Zarzar, A. Shastri, A. C. Balazs, J. Aizenberg, *Nature* **2012**, *487*, 214.